Enhanced Densification of Cavitated Dispersion-Strengthened Aluminum by Thermal Cycling

CHRISTOPHER SCHUH, BING Q. HAN, and DAVID C. DUNAND

We report experimental data of creep cavity shrinkage for dispersion-strengthened-cast aluminum with about 23 vol pct submicron Al_2O_3 dispersoids, annealed isothermally or subjected to thermal cycling without applied stress. Thermal cycling is found to increase the rate of densification by a factor of 3 to 5.5 relative to isothermal annealing at the upper cycling temperature, allowing for recovery of full theoretical density in a shorter time. Isothermal densification is discussed in light of a diffusive cavity shrinkage mechanism, and a model considering thermal mismatch stresses is employed to rationalize the enhanced rate of densification observed during thermal cycling. Intermittent thermal-cycling densification is shown to improve creep life of dispersion-strengthened aluminum through the suppression of tertiary damage accumulation processes.

I. INTRODUCTION

DESPITE their outstanding creep resistance, oxide-dispersion-strengthened aluminum materials have limited creep ductility due to the formation and subsequent growth and linkage of creep cavities. A recent investigation comparing the creep-rupture behavior of pure aluminum and various dispersion-strengthened aluminum alloys is given in Reference 1.

One approach to extending the creep life of various engineering components is *ex situ* treatments to close creep cavities. The technical literature contains many examples of the shrinkage and closure of cavities formed during deformation by isothermal heat treatment with or without superimposed hydrostatic pressure.[2–7] Although isothermal heat treatment at ambient pressure is simple and inexpensive, the time required to fully close creep cavities is often prohibitive. Hot isostatic pressing can more rapidly close porosity, but at an increased cost. Shiozawa and Weertman[8] showed that cavity shrinkage is strongly affected by the internal residual stress state, potentially increasing the rate of densification or causing cavity growth rather than shrinkage.

In the present article, we demonstrate that by thermally cycling dispersion-strengthened aluminum at ambient pressure, creep cavities can be eliminated more rapidly than by isothermal annealing. The enhanced densification rates observed during cycling are discussed in light of a diffusional densification model, giving special consideration to thermal-expansion-mismatch stresses. The effect of intermittent thermal-cycling treatments on the isothermal creep-rupture behavior of dispersion-strengthened aluminum is also investigated and discussed.

II. EXPERIMENTAL

The experimental material was as-cast dispersion-strengthened-cast aluminum (DSC-Al) with about 23 vol pct alumina dispersoids in a 99.9 pct pure Al matrix, from Chesapeake Composites Corp. (Newcastle, DE). Microstructural characteristics as well as ambient and elevated temperature mechanical properties of this material can be found in References 1 and 9 through 11. The dispersoid particles are approximately spherical with an average diameter of about 0.3 μm and are well dispersed in large matrix grains ($\sim$2 to 10 mm diameter).

A. Cavity Shrinkage Experiments

The specimens tested in these experiments were previously crept to failure at various temperatures and uniaxial tensile stresses in a separate study by Han and Dunand,[12] as shown in Table I. The gage pieces were separated from the heads with a diamond blade, and the material in the vicinity of the fracture surface (where cavitation may be more extensive) was also removed. The resulting cylindrical specimens were approximately 20 to 30 mm long, with diameters of about 4.7 mm. The volume fraction of reinforcement, f, as reported in Table I was determined prior to creep using the Archimedes method of density measurement in distilled water (as described in more detail subsequently) and the rule of mixtures, neglecting the small amount of casting porosity known to exist in these materials.[10]

The cavitated specimens were given various thermal treatments to assess the kinetics of creep-cavity shrinkage. These treatments were performed in a radiant furnace consisting of four symmetrically positioned line heaters, outfitted with two jets of argon gas, as shown in Figure 1. The combination of radiant heating and forced-convection cooling allowed for rapid thermal excursions, as described in the following paragraph. For purposes of thermal control, a small radial hole was drilled into the side of each specimen to a depth of about half the specimen diameter, into which a small-bead, rapid-response, type-K thermocouple was inserted. The hole and thermocouple bead were then covered with zirconia thermal insulation to minimize the effect of either radiative or convective heat flux from the heaters or argon jets, respectively. This procedure ensured that the recorded temperature was an accurate measurement of the specimen temperature. Closed-loop thermal control maintained the

CHRISTOPHER SCHUH, Graduate Student, and DAVID C. DUNAND, Associate Professor, are with the Department of Materials Science and Engineering, Northwestern University, Evanston, IL 60208. BING Q. HAN, Postdoctoral Researcher, formerly with the Department of Materials Science and Engineering, Northwestern University, is with the Department of Metallurgical Engineering, McGill University, Montreal, PQ, Canada H3A 2B2.
Manuscript submitted January 25, 2000.

Table I. Summary of Specimens Used in Present Study, Including Prior Creep History from Reference 11 and Current Experimental Conditions

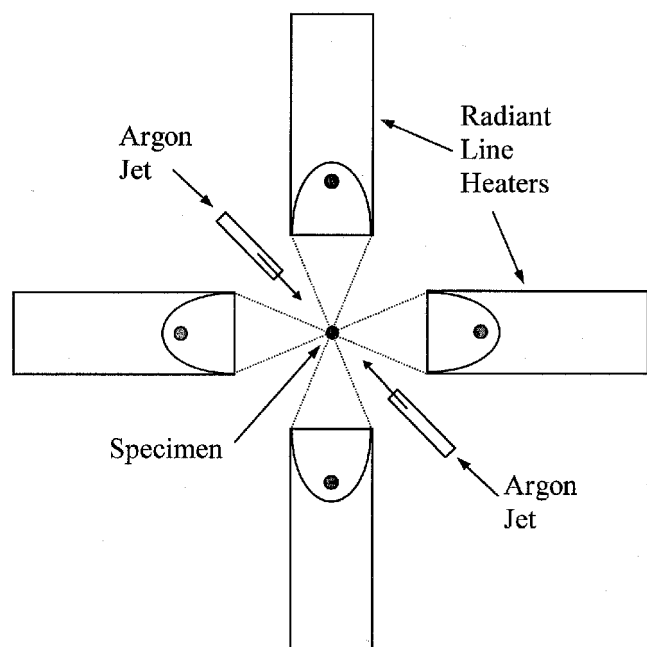| Specimen | Mass (g) | f | Prior Creep History | | | | Experiment in Present Work | |
			T (°C)	σ (MPa)	ε (Pct)	ρ	Thermal Treatment	Measurement
A1	1.154	0.232	400	69	4.8	0.982	351 °C, 1120 min	density
A2	1.167					0.981	200 °C to 400 °C, 1120 min	density
B1	1.062	0.215	400	81.5	6.8	0.981	400 °C, 1520 min	density
B2	1.068					0.979	200 °C to 400 °C, 1520 min	density
C	1.825	0.223	400	56.2	4.3	0.978	200 °C to 400 °C, 1200 min	density
D	3.157	0.237	370	56.2	2.8	0.987	200 °C to 400 °C, 2400 min	density and length
E	–	0.234	450	56.2	4.2	0.983	TEM	–

Fig. 1–Schematic of the apparatus used in isothermal and thermal-cycling heat treatments.

prescribed temperature to within ±2 K for most of the duration of each experiment, with maximum deviations of less than 10 K during rapid heating or cooling at the beginning and end of each stage of thermal treatment. On some specimens, a second thermocouple was attached in the same manner as the first, but at a different position along the gage length, to independently verify thermal uniformity to within ±5 K. The densification experiments are described individually below, and summarized in Table I. In all cases, the experiments were periodically interrupted by excursions to room temperature for density measurement, as described subsequently. All thermal cycles were triangular between 400 °C and 200 °C with ramp rates of 100 K/min.

(1) Specimens A and B: Two shorter specimens were prepared from each of these two failed creep specimens. One half was subjected to isothermal annealing (A1 at 351 °C and B1 at 400 °C), while the other half was thermally cycled (A2 and B2, 200 °C to 400 °C).
(2) Specimen C: This specimen was thermally cycled for comparison with specimens A2 and B2, all of which were originally crept at 400 °C but with different tensile stresses.

(3) Specimen D: This specimen was very long (62.16 mm), allowing for accurate measurement of linear shrinkage for comparison with the volumetric shrinkage (i.e., density) data.

The volume fraction of creep cavities was assessed by density measurement using the Archimedes method in distilled water. Water temperature was measured to within ±0.1 K, and the density of water corrected for temperature dependence using data from Reference 13. The relative error of the density measurements is estimated to be approximately 0.02 pct.

B. Microstructural Observations

In addition to the preceding densification experiments, one previously crept specimen (specimen E, Table I) was prepared for observation by transmission electron microscopy (TEM). Specimens with a thickness of approximately 0.5 mm were sectioned using a diamond saw and ground manually to a thickness of about 20 μm on grit papers. Disks with a diameter of 3 mm were then punched and thinned to perforation using a Gatan (Pleasanton, CA) dual ion mill operating at a voltage of 5 kV, a current of 1 mA, and an angle of 15 deg on a cold stage sample holder. The specimens were observed in a PHILIPS* 420 transmission electron microscope operating at 120 kV.

C. Intermittent Creep Experiment

The effect of cavity closure on the creep behavior of DSC-Al was investigated by an intermittent isothermal creep experiment. An as-cast tensile creep specimen with gage length of 50.3 mm and gage diameter of 4.67 mm was tested in air in a three-zone furnace at a constant temperature of 400 ± 1°C. After heating to the test temperature in about 15 minutes and soaking for 40 minutes, a tensile stress of 56.2 MPa was applied. The gage displacement was measured by an extensometer and a linear voltage displacement transducer with a resolution of 0.5 μm. At regular strain intervals of about 1 pct, the load was removed, heating was interrupted, and the specimen cooled to room temperature in about 2 hours. Following density measurement, the specimen was subjected to 100 thermal cycles between 200 °C and 400 °C, in the same fashion as specimens A2, B2, C, and D, as discussed earlier. The density of the cycled specimen was measured again and the preceding creep procedure repeated. This intermittent cycle of isothermal creep and

thermal-cycling annealing was repeated until the specimen failed.

The geometry of the creep specimen was such that the gage volume was about one-third of the total specimen volume. Therefore, at each stage of the experiment, the density of the gage section was calculated assuming that the specimen heads remained at the initial density of the specimen and did not develop cavities during creep. Additionally, although there was some initial casting porosity in the specimen heads,[10] this porosity was assumed nondensifying during thermal cycling. As discussed in Section III.D, this assumption is a source of error in the experimentally determined porosities.

III. RESULTS

A. Microstructural Observations

Three TEM micrographs shown in Figure 2 depict representative microstructural features of DSC-Al in the post-creep condition. As reported in previous articles,[10,11] the Al_2O_3 dispersoids are about 0.3 μm in diameter and generally equiaxed. In addition, many small cavities are observed in the crept gage section of DSC-Al. Figure 2(a) depicts a single cavity ~100 nm in diameter, located at the interface between the Al matrix and Al_2O_3 dispersoids; in this example, the cavity is noted to bridge the matrix between neighboring particles, so it lies on at least two Al/Al_2O_3 interfaces. Figures 2(b) and (c) illustrate additional cavities, which, in these projections, lie above or below their associated oxide particles. These micrographs further demonstrate that a single dispersoid may exhibit more than one cavity (Figure 2(b)) and that some of the cavities exhibit faceted surfaces (Figure 2(c)). The cavities found in the crept gage section of DSC-Al were invariably associated with neighboring dispersoid particles, suggesting that all of the observed cavities were located at Al/Al_2O_3 interfaces (as for the specific example seen in Figure 2(a)) and that these cavities were not preparation artifacts. Finally, the observed cavity sizes ranged from ~10 to ~180 nm.

B. Densification Kinetics

Figure 3 shows the relative density ρ of specimens A through D as a function of time, subjected to either isothermal or thermal cycling heat treatments. Although the average temperature during cycling was lower than 400 °C, the densification of thermally cycled specimens occurred more rapidly than for either isothermally annealed specimen. The measured density changes can be attributed entirely to volumetric shrinkage, as the mass of each specimen (Table I) was constant within 1 mg over the duration of the treatments. This observation rules out the possibility of density changes due to the accumulation of surface oxide.

Although the cavitated microstructures resulted from different sets of creep conditions (Table I), all of the specimens had similar initial relative densities, ranging between 0.978 and 0.987. In Figure 3, the densification curves of all four thermally cycled specimens are nearly coincident, and one specimen reached a relative density of unity after 1500 minutes, or 375 thermal cycles. In contrast, both isothermally treated specimens (351 °C and 400 °C) exhibited only small increases in relative density after similar times.
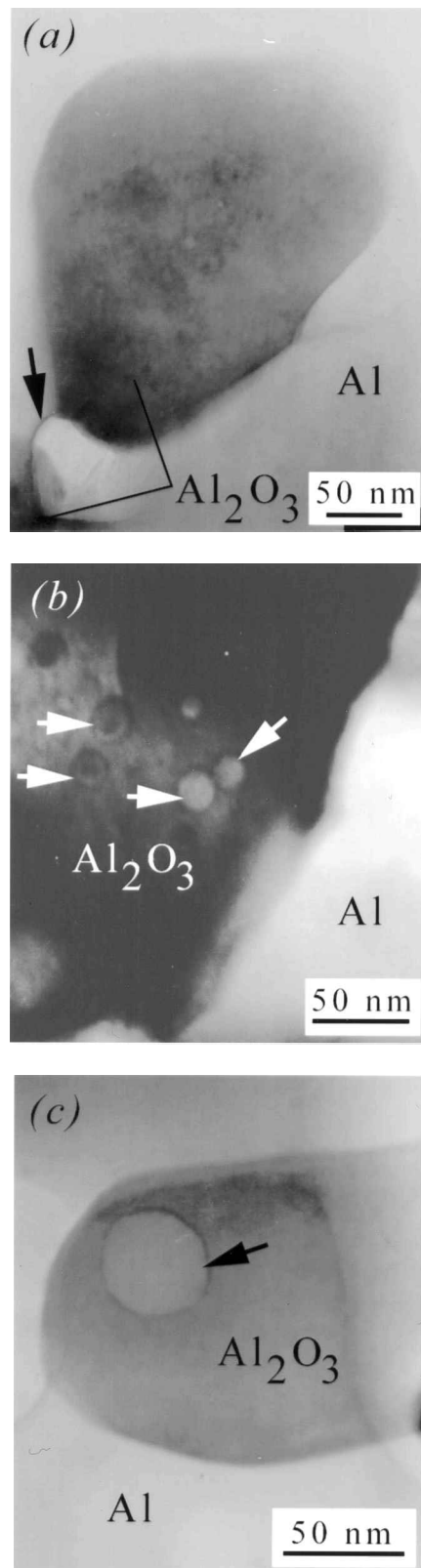

Fig. 2—(a) through (c) TEM micrographs of crept DSC-Al, specimen E (Table I), showing dispersoids of diameter ~0.3 μm and cavities of 10 to 100 nm noted by arrows.

For the discussion that follows, it is useful to determine the experimental densification rates, $\dot{\rho} = d\rho/dt$, from the experimental data. This is accomplished by fitting the data
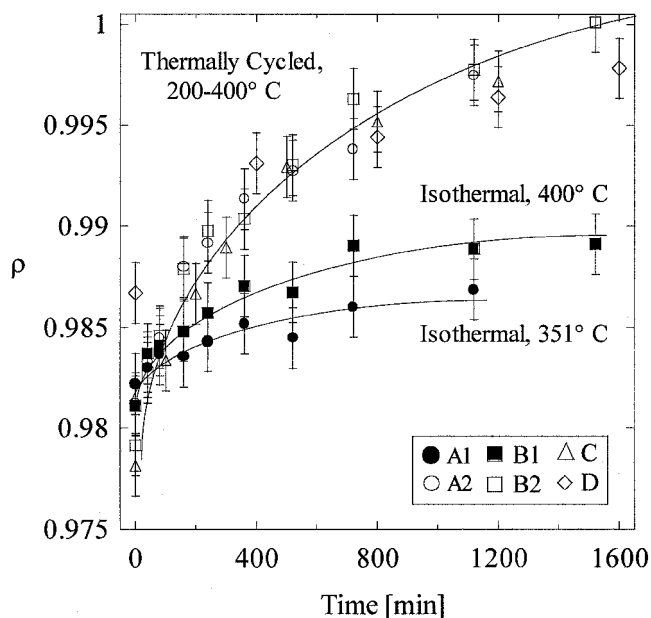
Fig. 3—Relative density ρ as a function of isothermal or thermal-cycling heat treatment time. Symbols correspond to specimen designations in Table I.
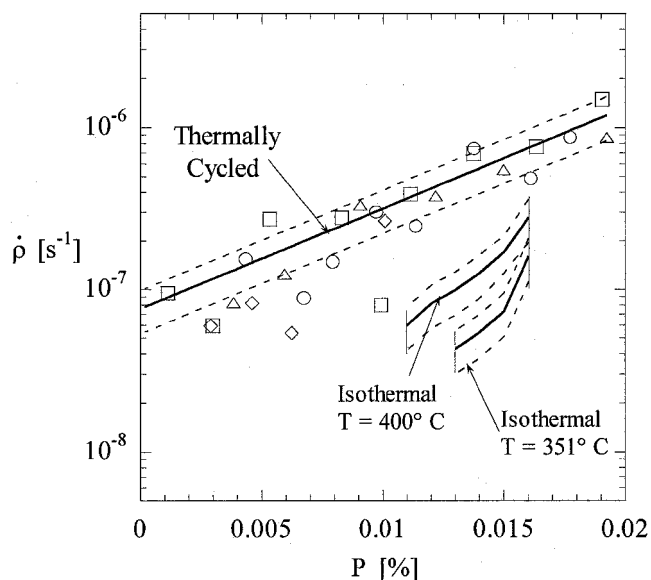

Fig. 4—Densification rates $\dot{\rho}$ as a function of porosity P during isothermal or thermal-cycling heat treatment of DSC-Al, with ±30 pct bounds shown in dashed lines. For the thermal-cycling experiments, data points (with the same symbols as in Fig. 3) are shown for comparison with the trendline determined from polynomial fitting.
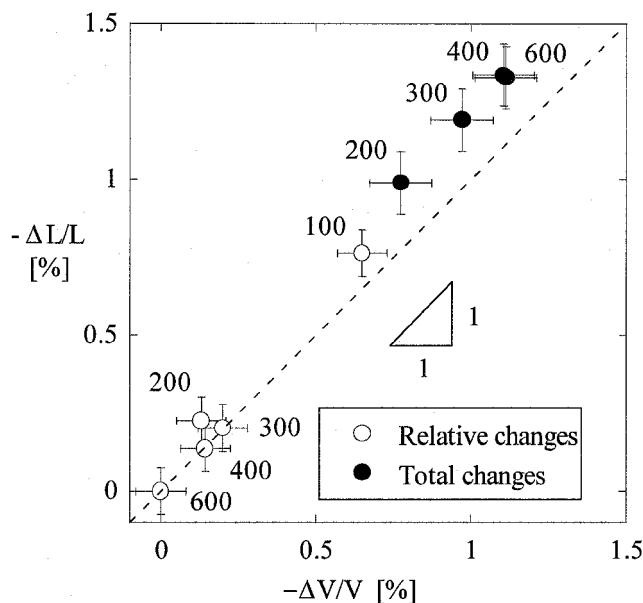

Fig. 5—Length and volume changes during thermal-cycling densification of specimen D (Table I). Filled symbols represent total changes relative to the initial length and volume of the specimen, and open symbols represent relative changes between successive stages of thermal cycling. The number of thermal cycles is labeled next to each point.

of Figure 3 with smooth polynomial functions, which are then differentiated to determine the densification rates. The results are shown in Figure 4 plotted against the specimen porosity, $P = 1 - \rho$, with estimated error bars of ±30 pct. For comparison, the density changes during thermal cycling experiments were also determined by calculating the slope between consecutive experimental data points in Figure 3, as shown by the data points in Figure 4. These data points and the band of densification rates determined from the polynomial fitting method are in general agreement. As illustrated by Figure 4, the densification rates for thermally

cycled specimens are notably larger than those for the isothermal specimens, with the enhancement increasing slightly at lower porosity.

C. Densification Shrinkage

Figure 5 shows the relationship between the linear shrinkage ($-\Delta L/L$) along the gage length (i.e., the direction of the applied stress during creep) and the volumetric shrinkage ($-\Delta V/V$) of specimen D, which was densified by thermal cycling. The volume change was calculated from the density measurements after each stage of thermal cycling. The solid points represent changes with respect to the initial condition of the specimen ($V_0 = 1.067$ cm^3 and $L_0 = 62.16$ mm), while the open points represent changes between subsequent stages of thermal cycling and density measurement. These two sets of points represent the same data and, therefore, are collinear. The slope of the data is unity within experimental error, with an intercept near zero.

The largest volumetric change observed during any stage of cycling was about 0.7 pct, corresponding to the first 100 thermal cycles, while subsequent sets of cycles resulted in smaller relative changes, as also shown in Figure 3. Figure 5 further shows that for each set of thermal cycles, the relative length change was nearly equal to the relative volume change of the specimen. Finally, when the specimen was fully dense and no additional volume shrinkage was detected, there was no additional length change either, corresponding to the datum point at the origin of Figure 5. This observation rules out thermal ratchetting as a possible contributor to densification.

D. Intermittent Creep Experiment

Figure 6 shows the creep curve obtained at 400 °C and 56.2 MPa for the intermittently cycled specimen, compared
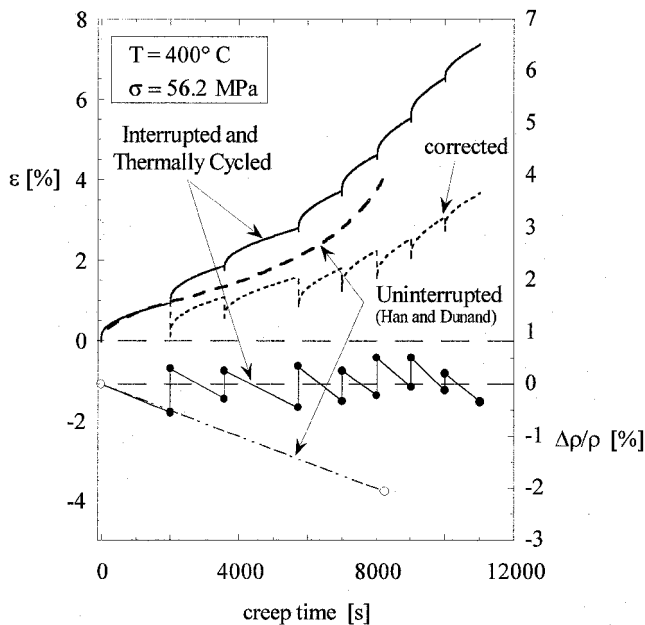
Fig. 6–Creep curves and relative density evolution for specimens that were crept to failure with (present study) and without (from Ref. 12) intermittent thermal cycling without applied stress. Also shown is the creep curve of the intermittently cycled specimen after correction for gage shrinkage during the cycling treatment.

with an uninterrupted creep test of the same material (as-cast DSC-Al) at the same stress and temperature. The several creep curves obtained during the intermittent test have been concatenated to reconstruct the full creep history. Also shown in Figure 6 are the relative density histories of the two specimens, which show that uninterrupted creep allows for the accumulation of several percent porosity at fracture, while intermittent cycling maintains the specimen density at a nearly constant level. Indeed, the density of the intermittently cycled specimen was, at several stages of the experiment, higher than the initial value. This result is probably due to the shrinkage of casting porosity present in the as-cast specimen before the creep test. Shrinkage and closure of casting porosity is not limited to the gage section of the specimen; this is a source of error in the determination of the gage porosity, which may increase over the several successive stages of the experiment.

As demonstrated in Figure 5, each stage of thermal cycling results in a contraction of the gage length, which has not been accounted for in the creep history of Figure 6. After each stage of thermal cycling, there is a shrinkage strain in the specimen gage, given by Figure 5 as

$$\varepsilon = -\Delta V/V \qquad [1]$$

Applying this correction to each stage in the intermittent creep history yields the dotted curve in Figure 6. This corrected creep history reflects the true specimen length at any given time during the experiment, while the uncorrected curve indicates the total tensile strain accumulated by creep.

The uninterrupted test and the intermittent thermal-cycling experiment both failed at true strains of about 4 pct, after accounting for the shrinkage accumulated during thermal cycling. However, the cycled specimen was able to sustain a larger amount of total creep strain (about 7.5 pct),

corresponding to a lifetime of 184 minutes, an increase of about one-third over the uninterrupted experiment.

IV. DISCUSSION

A. Kinetics of Cavity Shrinkage

As discussed in detail by Ashby and co-workers[14,15] in their treatment of "final stage" powder densification, there are three main mechanisms for cavity closure by sintering processes: boundary diffusion, volume diffusion, and creep. The purpose of the following discussion is to identify the dominant mechanism of densification during the present isothermal experiments. The effects of thermal cycling are then considered through the production of internal thermal mismatch stresses. Thus, the enhanced rate of densification observed experimentally is rationalized by combining densification theory with micromechanical calculations of thermal stress.

1. Microstructure and densification geometry

Previous high-temperature deformation studies of DSC-Al provide strong indirect evidence that creep cavities are located at the matrix/dispersoid interfaces.[1] First, Dunand et al.[1] examined creep-fracture surfaces of DSC-Al by scanning electron microscopy and observed dimpled surfaces, with dispersoids located at the base of the dimples. Second, Han and Dunand[12] have performed a detailed creep cavitation study on as-cast DSC-Al as well as cast and extruded DSC-Al by periodically interrupting isothermal creep experiments to measure the specimen density by the Archimedes method. They have found that cast DSC-Al, with millimeter-sized matrix grains, and extruded, recrystallized DSC-Al, with ~1-μm grains, exhibit the same rate of cavitation under identical creep conditions.[12] This result indicates that it is the total matrix/dispersoid interfacial area, and not the total grain boundary area, that controls cavity growth.[1] The TEM micrographs in Figure 2 agree with the preceding indirect evidence, showing ~10 to 100 nm cavities located at Al_2O_3 dispersoids. The TEM observations further indicate that a single dispersoid may be associated with multiple cavities (Figure 2(b)), and a single individual cavity may link two neighboring dispersoids (Figure 2(a)). As described in Reference 1, creep cavities in DSC-Al are located primarily at dispersoids in grain interiors, and grain boundary density plays a negligible role in cavitation during creep. Therefore, the closure of grain boundary cavities is of only minor importance relative to the closure of cavities in the grain interior.

For the discussion to follow, we relate the macroscopic relative density to the size of an average microscopic cavity through a simplified geometry based on the preceding microstructural observations. Cavities are taken as hemispherical (Figure 7(a)), with an average of N_c cavities coordinating each dispersoid at the dispersoid/matrix interface. The porosity and relative density of the composite can now be related to the average cavity radius, r, through

$$P \equiv 1 - \rho = \frac{2}{3} \cdot \pi \cdot N_c \left(\frac{r}{\lambda_p}\right)^3 \qquad [2]$$

where λ_p is the average center-to-center dispersoid spacing, which can be expressed as a function of the volume fraction and average diameter of dispersoids. The macroscopic densification rate, $d\rho/dt$, can then be expressed as a function of the microscopic cavity shrinkage rate $-dr/dt$:
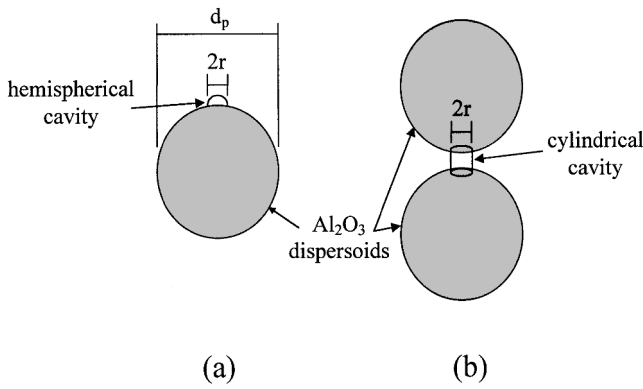
Fig. 7—Schematic representations of microstructural units: (a) hemispherical cavities decorate spherical dispersoid particles, and (b) cylindrical cavities bridge matrix ligaments to coordinate two dispersoids (Fig. 2(a)).

$$\dot{\rho} \equiv \frac{d\rho}{dt} = -2 \cdot \pi \cdot \frac{N_c}{\lambda_p^3} \cdot r^2 \cdot \frac{dr}{dt} \qquad [3a]$$

We note that changes in the specific assumptions regarding the arrangement of dispersoids, shape of the cavities, *etc.*, do not alter the important result that the densification rate is proportional to the average cavity shrinkage rate. For example, if the cavities are taken to be cylindrical with radius *r*, bridging the matrix between two dispersoids (Figure 2(a)), as shown schematically in Figure 7(b), then Eq. [3a] is replaced by

$$\dot{\rho} = -2 \cdot \pi \cdot \frac{(\lambda_p - d_p)}{\lambda_p^3} \cdot N_c \cdot r \cdot \frac{dr}{dt} \qquad [3b]$$

2. *Densification mechanisms*

Densification must proceed by the removal of vacancies from cavities to sinks or, equivalently, by the transport of atoms at external surfaces or grain boundaries to cavities. Thus, any process of atomic diffusion or nonconservative dislocation motion is a potential densification mechanism. In the present work, densification is time dependent (Figure 3), so processes of boundary or bulk diffusion as well as creep are of interest. There are several models of cavity shrinkage by each of these mechanisms,[15–18] which predict the cavity shrinkage rate as a function of the cavity radius, material parameters, and state variables. Since these mechanisms are limited by the kinetics of diffusion, they all incorporate a strong temperature dependence through an Arrhenius parameter:

$$\dot{\rho} \propto \exp\left(-\frac{Q}{R \cdot T}\right) \qquad [4]$$

where R is the gas constant, *T* is the absolute temperature, and *Q* is an activation energy for diffusion, which is characteristic of the dominant densification mechanism.

In the present investigation, only two isothermal densification temperatures were considered (351 °C and 400 °C), making experimental determination of *Q* only a rough estimate. However, densification rates are themselves density dependent, allowing the value of *Q* to be determined from Eq. [4] at each relative density over which the two data sets coincide. The two sets of experimental isothermal densification data (Figure 4) coexist over the range $\rho \approx 0.984$ to 0.987, about half of the full measured range $\rho \approx 0.983$ to

0.989. When *Q* is determined over this range using Eq. [4] with the fitted isothermal densification rates from Figure 4, values in the range $Q \approx 40$ to 65 kJ/mol are found.

This activation energy for densification is significantly below that of volume diffusion in aluminum ($Q_v = 142$ kJ/mol[19]), which would be characteristic of bulk-diffusional densification or power-law creep, were either of these the dominant mechanism of densification. Since diffusion of Al in dislocation cores occurs with $Q_d = 84$ kJ/mol,[19] even an extremely high dislocation density would not account for the experimentally measured temperature dependence of densification. The activation energy for grain-boundary diffusion in aluminum ($Q_{gb} = 82$ kJ/mol[19]) is also somewhat larger than the experimental value. Furthermore, with matrix grains in the millimeter-size range, diffusion along grain boundaries can be neglected as a significant contributor to cavity shrinkage.

Having established some reservations about the most common mechanisms of densification by virtue of a low experimental activation energy, we propose that the isothermal densification of DSC-Al is kinetically limited by diffusion of Al atoms along the interface between matrix and dispersoids. Although we know of no direct experimental evaluation of *Q* for Al/Al$_2$O$_3$ interfacial diffusion, this suggestion is supported by data of Hasegawa *et al.*,[20] who performed creep experiments on oxide dispersion-strengthened aluminum with a volume fraction of submicron alumina dispersoids similar to that of DSC-Al ($f = 0.22$) and matrix grains of about ~0.5 μm diameter. At high stresses (60 to 300 MPa), these authors identified a power-law creep regime with an activation energy characteristic of volume diffusion in Al ($Q \approx 145$ kJ/mol). At lower stresses (10 to 100 MPa), they observed deformation characteristic of grain- or phase-boundary sliding creep (*i.e.*, stress exponent of 2), but with an activation energy of $Q = 46 \pm 2$ kJ/mol, significantly below the activation energy for volume or grain-boundary diffusion in aluminum. This value was determined from data at five temperatures over the range 150 °C to 550 °C for each of four tensile stresses and, thus, has only a small experimental error bar.

Both the creep data of Hasegawa *et al.*[20] ($Q = 46 \pm 2$ kJ/mol) and the present densification data ($Q = 40$ to 65 kJ/mol) suggest the operation of a diffusional process with an anomalously low activation energy. Similar results have been found for diffusional creep of yttria-dispersion-strengthened magnesium[21] and for creep pushout of quartz and nickel fibers from a lead matrix.[22] We therefore conjecture that this low activation energy corresponds to diffusion of Al in the dispersoid/matrix interface. Given the position of cavities at Al$_2$O$_3$ interfaces (Figure 2), it is reasonable to consider a process in which vacancies are emitted from the cavity into the Al/Al$_2$O$_3$ interface, followed by interfacial diffusion to a pinned matrix dislocation. Since dispersoid particles are well-known sites of dislocation pinning (dislocations produced during creep or thermal cycling),[10] it is expected that a high dislocation density will be maintained during high-temperature annealing. In light of the high dislocation density and the large average distance from cavities to grain boundaries, dislocations are likely to be the dominant sink sites for vacancy annihilation.

Assuming that the preceding mechanism is indeed dominant during the isothermal densification of DSC-Al, the

model of Speight and Beere[23] gives the rate of shrinkage or growth of a cavity at a grain boundary:

$$\frac{\partial r}{\partial t} = \frac{4 \cdot \Omega \cdot \varphi \cdot \delta D_{0,b} \cdot \exp\left(-\dfrac{Q_b}{R \cdot T}\right)}{r^2 \cdot k \cdot T} \cdot \sigma^* \qquad [5]$$

in which Ω is the atomic volume of the diffusing species, $\delta D_{0,b}$ and Q_b are the pre-exponential constant and activation energy for boundary diffusion, respectively; k is Boltzmann's constant; and φ is a cavity spacing parameter. The above cavity growth rate has been formulated for a spherical cavity located on a grain boundary, which we adapt to the case of an axisymmetric cavity on the dispersoid/matrix interface by replacing the boundary diffusion parameters $\delta D_{0,b}$ and Q_b with analogous interfacial diffusion parameters, $\delta D_{0,i}$ and Q_i.

The rate of cavity growth or shrinkage depends on the normal stress at the boundary σ_b through the effective pressure σ^*:

$$\sigma^* = \sigma_b - \frac{n \cdot \gamma}{r} \qquad [6]$$

where γ is the surface energy of the matrix and negative stresses denote compression. The dimensionless constant $n = 2$ for the hemispherical void (Figure 7(a)) and $n = 1$ for the cylindrical void (Figure 7(b)). For the latter case of a cylindrical void, the densification rate (Eq. [5]) is also multiplied by a factor of 2, to account for the contribution of two interfaces in the diffusion problem. During isothermal annealing without external pressure, $\sigma_b = 0$ and the effective stress reduces to the thermodynamic term, $\sigma^* = -2\gamma/r$ or $-\gamma/r$, for hemispherical and cylindrical cavities, respectively. Although Eq. [5] was originally developed to explain cavity growth during tensile creep with applied stress σ_b normal to the boundary, it is equally valid for compressive stresses (negative values of σ_b) and, indeed, has been applied to the case of cavity closure by Riedel.[24]

Finally, the macroscopic shape changes observed in the specimen during densification (Figure 5) are related to the mechanism of densification, as described in the following. Since the cavities in DSC-Al were generated during tensile creep experiments, they are expected to lie on interfaces oriented nearly perpendicular to the applied tensile stress.[24] During densification by the above interface-diffusion mechanism, vacancies are emitted by the cavity directly into the interface, which results in contraction of the material in the prior tensile direction. This model thus predicts no significant contractions in the perpendicular directions, with all of the volume change during densification accommodated by linear shrinkage in the gage direction. This is indeed the behavior observed during the present thermal-cycling densification experiments (Figure 5).

3. Thermal mismatch stresses

Thermal cycling is anticipated to impact the densification rate through the production of thermal-expansion mismatch stresses between matrix and particles, which affect σ_b in Eq. [6]. Since the thermal expansion coefficients of Al and Al_2O_3 differ by about a factor or 3 (Table II), internal mismatch stresses may be substantial during cycling. For interfacial diffusion, the densification rate depends only upon the stress normal to the interface,[25] which can be readily estimated

from micromechanics calculations, as described in the following.

There are several micromechanical models that predict the internal stress state during thermal excursion of a particle-reinforced composite.[26–29] In general, these methods rely upon the Eshelby equivalent inclusion method[30] to assess the average stresses in spherical particles. The "generalized self-consistent model" of Park and Earmme[29] considers thermal dilatation of a spherical reinforcement particle surrounded by a concentric shell of matrix material, embedded in a matrix with thermal and elastic properties of the bulk composite material. For this case, the principal stress components in the inclusion are all equal and given by

$$\sigma_i = \frac{3 \cdot K_m \cdot K_i \cdot (\alpha_m - \alpha_i) \cdot (T - T_0)}{f \cdot (K_m - K_i)}$$
$$\cdot \left[f - \frac{K_i \cdot (K_m - K_e)}{K_e \cdot (K_m - K_i)} \right] \qquad [7]$$

where K is the bulk modulus; α the thermal expansion coefficient; T_0 the absolute temperature at which there is no thermal mismatch, and where the matrix and inclusion (dispersoid) properties are denoted by subscripts of m and i, respectively. As shown in Reference 29, the preceding equation places physical bounds on the particle stresses through the parameter K_e, which is the effective bulk modulus of the composite material. The Hashin–Shtrikman bounds on K_e are[31,32]

$$K_e^+ = K_i + (1 - f) \cdot \left[\frac{1}{K_m - K_i} + \frac{3 \cdot f}{3 \cdot K_i + 4 \cdot G_i} \right]^{-1} \qquad [8]$$

in the upper bound, and

$$K_e^- = K_m + f \cdot \left[\frac{1}{K_i - K_m} + \frac{3 \cdot (1 - f)}{3 \cdot K_m + 4 \cdot G_m} \right]^{-1} \qquad [9]$$

in the lower bound, where G is the shear modulus of the subscripted phase. Park and Earmme[29] have shown that these bounds on K_e are appropriately used in Eq. [7] in the limits of $f = 1$ (Eq. [8]) and $f = 0$ (Eq. [9]) and that these bounds match exactly those predicted by Kreher[27] using a variational method.

At room temperature, Redsten et al.[11] have shown that the Young's modulus of DSC-Al lies between the bounds established by Eqs. [8] and [9] somewhat closer to the upper bound. In the calculations to follow, we assume that this relative positioning of the composite modulus with respect to the Hashin–Shtrikman bounds holds at elevated temperatures and is given by

$$K_e = K_e^- + \frac{2}{3} \cdot (K_e^+ - K_e^-) \qquad [10]$$

where the value two-thirds is chosen according to the experimental Young's modulus data.[11]

Use of Eq. [10] in Eq. [7] thus predicts the average principal stress in the Al_2O_3 dispersoids for a thermal excursion from a stress-free temperature, T_0. Since creep relaxation of mismatch stresses occurs more rapidly at high temperatures, and since most of the specimens densified in this study were previously crept at 400 °C for long times during which thermal mismatch could relax (Table I), it is a reasonable

Table II. Materials and Microstructural Parameters Used in the Analytical Models*

Property	Al	Al$_2$O$_3$	Reference
Shear modulus, G (GPa)	$25.4 \cdot \left(1 - 0.5 \cdot \dfrac{T-300}{933}\right)$	$155 \cdot \left(1 - 0.35 \cdot \dfrac{T-300}{2320}\right)$	19
Poisson's ratio, ν	0.33	0.24	28
Thermal expansion coefficient, α (10^{-6} K^{-1})	$9.4 + 0.033 \cdot T$	8	40
Surface energy, γ (J/m^2)	1	–	39
Burger's vector, b (m)	$2.86 \cdot 10^{-10}$	–	19

*Bulk modulus is calculated using K $= 2G(1 + \nu)/3(1 - 2\nu)$.[38] Thermal expansion coefficients are fitted over the range 200 °C to 400 °C
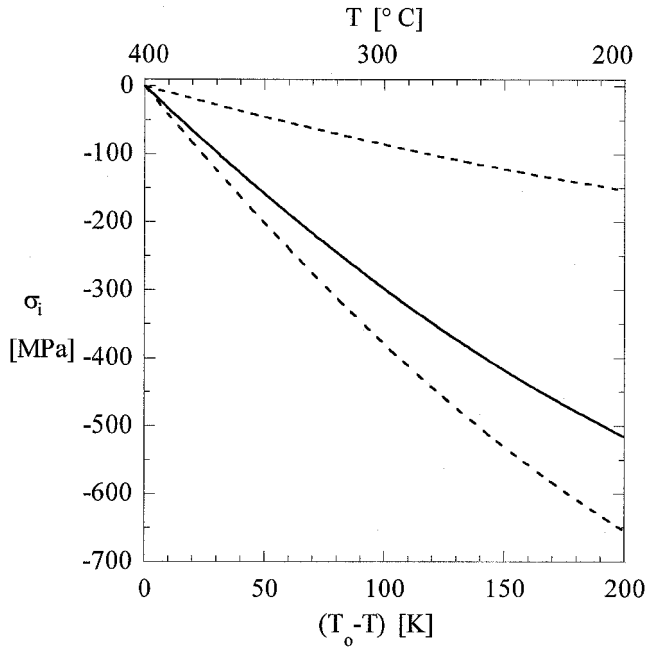

Fig. 8–Principal stresses in alumina-dispersoid particles during thermal cycling from upper temperature T_0, as calculated from Eq. [7] using the average bulk modulus from Eq. [10] (solid line). The upper and lower bounds (dashed lines) are computed using bulk moduli from Eqs. [8] and [9], respectively.

assumption to take the upper-cycling temperature (400 °C) as T_0. The use of Eq. [7] in these stress calculations requires that the presence of cavities at the particle/matrix interface be neglected, an implicit assumption that is considered reasonable if the cavity size and volume fraction are small compared to those of the dispersoid particles. Using the temperature-dependent physical properties of pure aluminum and alumina given in Table II, the calculated internal particle stresses are shown for the thermal-cycling temperatures (200 °C to 400 °C) in Figure 8. The resulting inclusion stress is compressive and nearly linear in T for the temperatures of interest during the thermal cycling experiments (200 °C to 400 °C) and can be reasonably expressed by

$$\sigma_i = -\kappa_1 \cdot (T_0 - T) + \kappa_2 \cdot (T_0 - T)^2 \qquad [11]$$

with $\kappa_1 = 3.4$ MPa/K and $\kappa_2 = 4 \cdot 10^{-3}$ MPa/K^2. Due to the large thermal expansion mismatch ($\sim 2 \times 10^{-5}$ K^{-1} on average) the particle stresses during thermal cycling are substantial. For comparison, the upper- and lower-bound stresses calculated using Eq. [7] with Eq. [8] or Eq. [9], respectively, are also shown in Figure 8.

In the generalized self-consistent model described previously, interparticle stress interactions are accounted for through the use of bulk composite properties, so the average normal stress on the interface is equal to any principal stress in the inclusion:

$$\sigma_b = \sigma_i \qquad [12]$$

From Figure 8 and Eq. [12], the predicted interfacial stresses vary during thermal cycling, between a stress-free state at the upper temperature and compressive stresses at lower temperatures. Such compressive stresses are expected to increase the cavity shrinkage rate; the magnitude of this increase during our thermal cycles will be assessed in Section 4.

Before proceeding, we note that the calculated internal stresses due to thermal mismatch are large, exceeding the stress required for slip in pure aluminum.[19] However, because of the fine scale of the dispersoid particles, we expect dislocation motion to be suppressed in these materials,[9,33] allowing for local elastic stresses far greater than those required for slip. During the first several thermal cycles, thermal mismatch is probably accommodated by punching of prismatic dislocation loops.[34,35] After several cycles, such dislocations would tend to form tangled networks near the dispersoid particles, yielding a high dislocation density and a work hardened matrix.[34] The increase in matrix yield strength $\Delta\sigma$ due to work hardening can be determined from

$$\Delta\sigma = 1.25 \cdot G \cdot b \cdot \rho^{1/2} \qquad [13]$$

where G and b are the matrix shear modulus and Burger's vector, respectively; and ρ is the dislocation density developed during thermal cycling. Using the properties of aluminum in Table II and physically reasonable dislocation densities $\rho = 10^{15}$ to 10^{16} m^{-2}, Eq. [13] gives $\Delta\sigma = 245$ to 775 MPa. It is likely that such high dislocation densities would be developed in DSC-Al after only a few thermal cycles. A work-hardened matrix with a high yield stress is thus expected during most of the thermal cycles, leading to elastic accommodation of thermal-expansion mismatch. The lack of macroscopic plastic deformation, or strain ratcheting, after many thermal cycles (point at the origin in Figure 5) also implies that matrix plasticity is suppressed during thermal cycling. Finally, since the thermal cycles were rapid, and the largest stresses are developed at the lower cycling temperatures, it is further reasonable to neglect relaxation of mismatch stresses by diffusional creep.

4. Densification enhancement during thermal cycling

In Figure 4, the densification rates measured during thermal cycling exceed those measured in the isothermal experiments, even when comparing to isothermal densification at the upper cycling temperature. The true densification enhancement during thermal cycling is best discussed by considering the effective average temperature during cycling, which can be found by averaging the Arrhenius parameter (Eq. [4]) over a full thermal cycle.[36] However, given the limited isothermal densification data for DSC-A1, we define the enhancement factor, δ, as the ratio of the densification rate during cycling to that at the upper cycling temperature. Experimentally, the data in Figure 4 give values in the range $\delta \approx 3$ to 5.5, over the porosity range $P = 1.1$ to 1.6 pct. Taking extreme values of $\dot{\rho}$ within the experimental error bands would somewhat reduce or increase this value.

The densification model of Eq. [5], together with the internal stress calculations summarized in Eqs. [11] and [12], provide a foundation from which to predict the densification enhancement during thermal cycling. The proportionality between macroscopic densification rate and microscopic cavity shrinkage rate (Eqs. [3]) allows δ to be calculated directly from Eq. [5], giving

$$\delta = \frac{\dfrac{1}{\Delta T} \displaystyle\int_{\Delta T} \dfrac{1}{T} \cdot \exp\left(\dfrac{-Q_i}{R \cdot T}\right) \cdot \left(\sigma_{\mathbf{b}}(T) - \dfrac{n \cdot \gamma}{r}\right) \cdot dT}{\dfrac{1}{T_0} \cdot \exp\left(\dfrac{-Q_i}{R \cdot T_0}\right) \cdot \left(\dfrac{n \cdot \gamma}{r}\right)} \quad [14]$$

The integral form of the numerator in the this expression represents the average densification rate during a complete thermal cycle over the temperature range ΔT. With the boundary stress $\sigma_{\mathbf{b}}(T)$ as given by Eqs. [11] and [12], the preceding equation can be evaluated at a selected cavity radius r.

Figure 9 shows the predicted values of δ calculated from Eq. [14], using the activation energy $Q = 46$ kJ/mol and γ from Table II, over a physically reasonable range of cavity radii. The predictions can be compared with the horizontal band in the figure, which indicates the range of values measured experimentally. For larger cavity radii, the model predicts enhancement factors similar to or larger than those found by experiment, particularly if the cylindrical void geometry is used. At smaller cavity sizes, the predicted enhancement diminishes, as the thermodynamic sintering stress ($n\gamma/r$) increases relative to the thermal mismatch stresses. However, very small cavities are expected to sinter and disappear rapidly, leaving the largest cavities (e.g., $r \geq 75$ nm) to control the kinetics of densification. Therefore, because they limit the densification process, it may be more reasonable to consider the shrinkage of these larger cavities when modeling the densification of a distribution of cavity sizes. Finally, we note that the average spacing between adjacent dispersoids in DSC-Al is about 90 nm; cavities near this size or larger are thus expected to contact two dispersoids, roughly in the cylindrical cavity geometry shown in Figure 7(b). The shrinkage of large cylindrical cavities may then limit the densification process.

The success of Eq. [14] in predicting enhancements within the experimentally observed range indicates that thermal mismatch stresses are sufficient to fully account for the observed densification enhancement during thermal cycling.
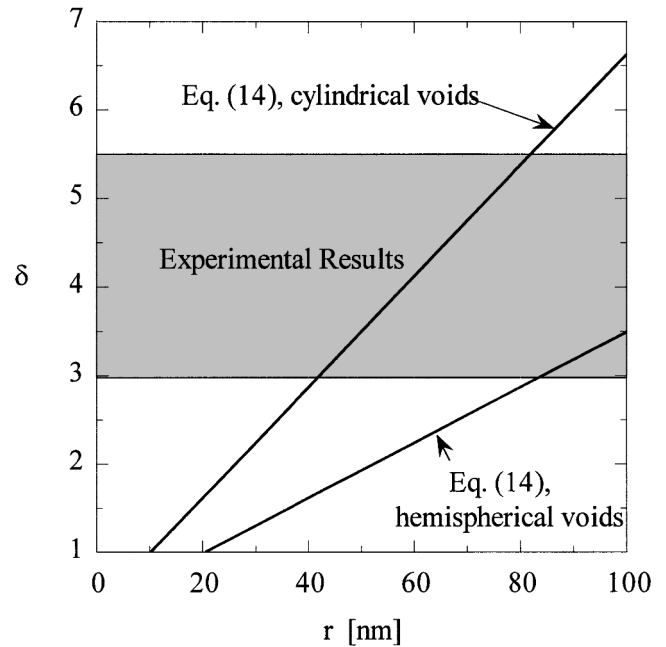

Fig. 9–Enhancement factor δ, relating the densification rate during thermal cycling to that at the upper cycling temperature, as a function of the cavity radius r. The range of experimental values is denoted by the shaded band and compared with predictions of Eq. [14].

Given additional assumptions about the microstructural dimensions and the cavity spacing, the approach described above can also be used to predict absolute values of the densification rate during thermal cycling, in addition to the enhancement factor δ.[37]

Although the interfacial-diffusion mechanism considered in the present work appears sufficient to explain many features of both isothermal and thermal-cycling densification of DSC-Al, additional mechanisms may contribute to the total densification rate. Particularly, when large internal stresses are present, one might expect a change of dominant densification mechanism to, e.g., lattice diffusion or matrix creep-controlled densification. Since the matrix stress state that affects these mechanisms (due to thermal expansion mismatch) is quite complex, we make no effort to predict their contributions here. However, for different multiphase composite materials or different cavity positions relative to the reinforcing phase, such mechanisms could be of primary importance.

B. Rejuvenation of Crept DSC-Al by Thermal Cycling

The larger time-to-failure of the intermittently thermally cycled creep specimen (Figure 6) demonstrates that periodic cycling treatments can improve the creep performance of DSC-Al. Figure 10 shows the creep rate, $\dot{\varepsilon} = d\varepsilon/dt$, plotted against the accumulated true strain, ε, for both of these specimens. The curve for the uninterrupted specimen is typical of reinforced aluminum materials; following a stage of primary creep, a brief minimum creep rate is observed, with a subsequent acceleration to failure (tertiary creep). The increase in creep rate prior to failure is due to the accumulation of cavitation damage, which prohibits a steady state from being established.[10] In contrast to this typical behavior,
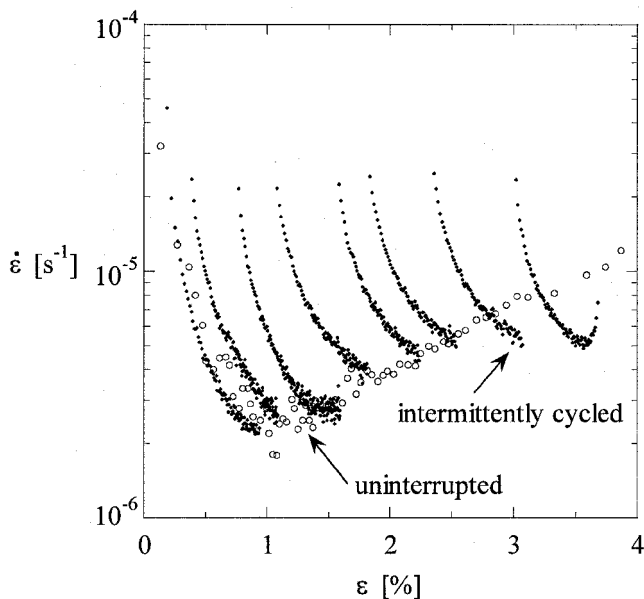
Fig. 10—Tensile creep rate $\dot{\varepsilon}$ as a function of accumulated strain ε, for an intermittently cycled specimen, as well as for a DSC-Al specimen subjected to uninterrupted creep (from Ref. 12).

intermittent thermal cycling treatment prevented the development of extensive cavitation damage (Figure 6) and, therefore, prolonged the acceleration of tertiary creep. It is interesting to note that in the intermittently cycled specimen, fracture occurred without significant accumulation of cavity volume. This result suggests that creep fracture in DSC-Al need not be associated with total cavity volume but may be controlled by, e.g., total debonded interfacial area or the maximum defect dimension.

The preceding results on DSC-Al are consistent with many previous reports of creep-life improvement by sintering.[2,3,4] However, as shown in Figures 3 and 4, isothermal densification is prohibitively slow for this kind of rejuvenation treatment in DSC-Al. The more rapid thermal-cycling densification procedure may thus offer a less costly alternative to hot isostatic pressing for this purpose.

V. CONCLUSIONS

Shrinkage of creep cavities by thermal treatment was examined in DSC-Al, a dispersion-strengthened aluminum containing approximately 23 pct submicron alumina dispersoids. Isothermal annealing at either 351 °C or 400 °C resulted in only small density changes, while a thermal-cycling treatment with 4-minute thermal cycles between 200 °C and 400 °C (without applied stress) produced more rapid densification, allowing for full recovery of pre-creep density. Densification rates during thermal cycling were higher by about a factor of 3 to 5.5 than those observed during isothermal densification at the maximum cycling temperature.

Based on the activation energy of the isothermal densification process, the dominant mechanism of densification is thought to be diffusion along the Al/Al_2O_3 interface. The diffusive flux is enhanced by compressive stresses on the dispersoid/matrix interface, which evolve during thermal cycling due to thermal expansion mismatch. Using an existing micromechanical model to determine the internal stress state, we find that this mechanism may indeed account for the observed densification enhancement during thermal cycling.

Since the closure of small amounts of closed porosity is typically the most time-consuming stage of sintering processes, accelerated densification by thermal cycling may have practical applications. We demonstrate that intermittent thermal cycling DSC-Al without external load enhances the creep life by about 35 pct at 400 °C and 56.2 MPa. By suppressing the formation and/or growth of creep cavities, the onset and acceleration of tertiary creep are delayed.

REFERENCES

1. D.C. Dunand, B.Q. Han, and A.M. Jansen: *Metall. Mater. Trans. A,* 1999, vol. 30A, pp. 829-38.
2. A. Varloteaux, J.J. Blandin, and M. Suery: *Mater. Sci. Technol.*, 1989, vol. 5, pp. 1109-17.
3. P.W. Davies, J.P. Dennison, and H.E. Evans: *J. Inst. Met.*, 1966, vol. 94, pp. 270-75.
4. P.W. Davies, J.P. Dennison, and H.E. Evans: *J. Inst. Met.*, 1967, vol. 95, pp. 231-34.
5. H. Iwasaki, Y. Yada, T. Mori, M. Mabuchi, and K. Higashi: *Scripta Mater.*, 1996, vol. 34, pp. 1179-84.
6. N. Ridley, D.W. Livesey, and A.K. Mukherjee: *Metall. Trans. A*, 1984, vol. 15A, pp. 1443-50.
7. H. Iwasaki, T. Mori, M. Mabuchi, and K. Higashi: *Mater. Sci. Eng.*, 1998, vol. A242, pp. 32-38.
8. K. Shiozawa and J.R. Weertman: *Acta Metall.*, 1983, vol. 31, pp. 993-1004.
9. A.M. Jansen and D.C. Dunand: *The Johannes Weertman Symp.*, R.J. Arsenault, D. Cole, T. Gross, G. Kostorz, P. Liaw, S. Parameswaran, and H. Sizek, eds., TMS, Warrendale, PA, 1996, pp. 69-80.
10. A.M. Jansen and D.C. Dunand: *Acta Mater.*, 1997, vol. 45, pp. 4583-92.
11. A.M. Redsten, E.M. Klier, A.M. Brown, and D.C. Dunand: *Mater. Sci. Eng.*, 1995, vol. A201, pp. 88-102.
12. B.Q. Han and D.C. Dunand: Northwestern University, Evanston, IL, unpublished research, 1998
13. *Perry's Chemical Engineer's Handbook*, D.W. Green and J.O. Maloney, eds., McGraw-Hill, New York, NY, 1984.
14. E. Arzt, M.F. Ashby, and K.E. Easterling: *Metall. Trans. A*, 1983, vol. 14A, pp. 211-21.
15. A.S. Helle, K.E. Easterling, and M.F. Ashby: *Acta Metall.*, 1985, vol. 33, pp. 2163-74.
16. T. Shibutani, T. Kitamura, and R. Ohtani: *Metall. Mater. Trans. A*, 1998, vol. 29A, pp. 2533-42.
17. D.S. Wilkinson and M.F. Ashby: *Acta Metall.*, 1975, vol. 23, pp. 1277-85.
18. G.C. Kuczynski: *Acta Metall.*, 1956, vol. 4, pp. 58-61.
19. H.J. Frost and M.F. Ashby: *Deformation-Mechanism Maps: The Plasticity and Creep of Metals and Ceramics*, Pergamon Press, Oxford, United Kingdom, 1982.
20. T. Hasegawa, K. Minami, and T. Miura: in *Creep and Fracture of Engineering Materials and Structures*, B. Wilshire and R.W. Evans, eds., The Institute of Metals, London, 1990, pp. 159-68.
21. B.Q. Han and D.C. Dunand: in *Creep Behavior of Advanced Materials for the 21st Century*, R.S. Mishra, A.K. Mukherjee, and K.L. Murty, eds., TMS, Warrendale, PA, 1999, pp. 149-58.
22. J.V. Funn and I. Dutta: *Acta Mater.*, 1999, vol. 47, pp. 149-64.
23. M.V. Speight and W. Beere: *Met. Sci.*, 1975, vol. 9, pp. 190-91.

24. H. Riedel: *Fracture at High Temperature*, Springer-Verlag, Berlin, 1987.
25. A.C.F. Cocks and M.F. Ashby: *Progr. Mater. Sci.*, 1982, vol. 27, pp. 189-244.
26. K.K. Chawla: *Ceramic Matrix Composites*, Chapman & Hall, London, 1993.
27. W. Kreher: *J. Mech. Phys. Solids*, 1990, vol. 38, pp. 115-28.
28. T.W. Clyne and P.J. Withers: *An Introduction to Metal Matrix Composites*, Cambridge University Press, Cambridge, United Kingdom, 1993.
29. S.J. Park and Y.Y. Earmme: *J. Composite Mater.*, 1999, vol. 33, pp. 1205-21.
30. J.D. Eshelby: *Proc. R. Soc. London*, 1957, vol. A241, pp. 376-96.
31. Z. Hashin and S. Shtrikman: *J. Mech. Phys. Solids*, 1963, vol. 11, pp. 127-40.
32. Z. Hashin: *J. Appl. Mech.*, 1983, vol. 50, pp. 481-505.
33. D.C. Dunand and A.M. Jansen: *Acta Mater.*, 1997, vol. 45, pp. 4569-81.
34. D.C. Dunand and A. Mortensen: *Acta Metall. Mater.*, 1991, vol. 39, pp. 127-39.
35. R.J. Arsenault and N. Shi: *Mater. Sci. Eng.*, 1986, vol. 81, pp. 175-87.
36. D.C. Dunand and C.M. Bedell: *Acta Mater.*, 1996, vol. 44, pp. 1063-76.
37. C. Schuh, B.Q. Han, and D.C. Dunand: *Symp. to Honor Julia R. Weertman*, Y. Chung, D.C. Dunand, P.K. Liaw, and G.B. Olson, eds., TMS, Warrendale, PA, 1999, pp. 81-93.
38. T.H. Courtney: *Mechanical Behavior of Materials*, McGraw-Hill, New York, NY, 1990.
39. J. Harper and J.E. Dorn: *Acta Metall.*, 1957, vol. 5, pp. 654-65.
40. *Thermal Expansion: Metallic Elements and Alloys*, Y.S. Touloukian, R.K. Kirby, R.E. Taylor, and P.D. Desai, eds., Plenum, New York, NY, 1975.